Dynamic ocean redox conditions during the end-Triassic mass extinction: Evidence from pyrite framboids

Jing Li[a], Huyue Song[a*], Li Tian[a], David P.G. Bond[b], Haijun Song[a], Yong Du[a], Chi Zhang[a], Daoliang Chu[a], Paul B. Wignall[c], Jinnan Tong[a]

[a] State Key Laboratory of Biogeology and Environmental Geology, School of Earth Sciences, China University of Geosciences, Wuhan, 470073, Hubei Province, P.R. China

[b] School of Environmental Science, University of Hull, Hull, HU6 7RX, United Kingdom

[c] School of Earth and Environment, University of Leeds, Leeds, LS2 9JT, United Kingdom

* Corresponding Author. *E-mail address:* hysong@cug.edu.cn

Abstract

The end-Triassic (~201 Mya) records one of the five largest mass extinction events of the Phanerozoic. Extinction losses were coincident with large igneous province volcanism in the form of the Central Atlantic Magmatic Province (CAMP) and major carbon isotope excursions (CIEs), suggesting a link between these phenomena. Marine anoxia has been implicated as a causal factor in the crisis, but there remains some uncertainty regarding the role of marine redox changes in marine extinction phases because both intensity and duration of marine anoxia are poorly constrained. We employ high resolution pyrite framboid size-frequency analysis at two Triassic-Jurassic (Tr-J) boundary sections: Kuhjoch in Austria (the Tr-J Global Boundary Stratotype Section and Point; GSSP) and St. Audrie's Bay in England (former GSSP candidate) in order to further evaluate the role of marine anoxia in the end-Triassic mass extinction (ETME). The St. Audrie's Bay section records predominantly anoxic conditions punctuated by weakly oxygenated (dysoxic) conditions through the Tr-J transition, even during shallow-water intervals. Kuhjoch experienced both anoxic and dysoxic conditions during the ETME but became better oxygenated near the Tr-J boundary. Marine anoxia is therefore implicated in the extinction at both locations. A similar redox history is known from the Central European Basin, Western Tethys and Panthalassa, where marine anoxia developed in the lead up to the ETME prior to reoxygenation around the Tr-J boundary.

Key words: Marine anoxia, Central Atlantic Magmatic Province, End-Triassic mass extinction, Pyrite framboids

1. Introduction

The end-Triassic mass extinction (ETME) is one of the five great biodiversity crises of the Phanerozoic: conodonts went extinct, whilst corals, ammonites, bivalves, demosponges and brachiopods experienced severe losses (Hallam and Wignall, 1997; Pálfy et al., 2000; Hillebrandt et al., 2013; Song et al., 2018; Wignall and Atkinson, 2020). Low latitude marine taxa suffered preferential losses (Kiessling et al., 2007) and terrestrial ecosystems were not immune as widespread losses amongst tetrapods paved the way for a world dominated by dinosaurs (e.g. Olsen et al., 2002).

The voluminous eruptions of the Central Atlantic Magmatic Province (CAMP) are considered to be the ultimate driver of extinction (Schoene et al., 2010; Ruhl et al., 2011; Davis et al., 2017; Lindström et al., 2021). The emplacement of the CAMP has been implicated in a major increase in atmospheric $p\mathrm{CO}_2$ (McElwain et al., 1999; Beerling and Berner, 2002; Bonis et al., 2010b; Steinthorsdottir et al., 2011), ocean acidification (Hautmann et al., 2004; Greene et al., 2012), widespread marine anoxia (Bonis et al., 2010a; Schoepfer et al., 2016; Jost et al., 2017; Luo et al., 2018; He et al. 2020, 2022a,b), photic zone euxinia (PZE; Jaraula et al., 2013; Kasprak et al., 2015; Beith et al., 2021; Fox et al., 2022a) and global warming (McElwain et al., 1999; Kasprak et al., 2015; Schoepfer et al., 2016; Song et al., 2021; Yager et al., 2021). Contemporaneous sedimentary mercury anomalies (Thibodeau et al., 2016; Percival et al., 2017; Kovács et al., 2020) provide indirect evidence for this volcanism and suggest the CAMP eruptions were a key driver of environmental changes. Charcoal and polycyclic aromatic hydrocarbon records are indicative of wildfires (Marynowski and Simoneit, 2009; Belcher et al., 2010; Petersen and Lindström, 2012; Fox et al., 2022b; Kaiho et al., 2022) and there is evidence for volcanism-induced mutagenesis (e.g., Lindström et al., 2019) and soil erosion (e.g., van de Schootbrugge et al., 2020) which together are considered to reflect the terrestrial manifestation of the ETME.

Several studies have implicated anoxia in the ETME as suggested by the records of nitrogen, sulfur and uranium isotopes (Schoepfer et al., 2016; Jost et al., 2017; He et al., 2020), elemental redox proxies (Pálfy and Zajzon, 2012; He et al., 2022a,b), and the deposition of organic-rich mudrocks (Wignall, 2001a; Wignall et al., 2007) although such lithologies are by no means ubiquitous. However, evidence from some shallow water sites (e.g., Larne Basin, Northern Ireland) suggests that only weakly dysoxic conditions developed during the extinction crisis (Bond et al., 2022). Biomarkers of green sulfur bacteria (e.g., isorenieratane) indicate PZE but such evidence is often derived from the strata immediately above the extinction levels (Richoz et al., 2012; Jaraula et al., 2013; Kasprak et al., 2015; Beith et al., 2021; Fox et al., 2022a). Studies focusing on redox changes at the GSSP for the Tr-J boundary (Kuhjoch, Austria) are scarce (Pálfy and Zajzon, 2012), and the geographical and temporal extent of oxygen restriction globally remains relatively poorly constrained.

Pyrite framboids form near the redox boundary and the variability of their population sizes provides a robust method for the reconstruction of redox conditions in deep time (Wilkin et al., 1996; Wignall and Newton, 1998) and has been successfully applied in several extinction studies (e.g., Bond and Wignall, 2010; Wignall et al., 2010; Dai et al., 2018; Huang et al., 2019; Atkinson and Wignall, 2019). Currently, pyrite framboid studies across the Tr-J transition are either of low-resolution (Wignall, 2001; Wignall et al., 2010) or are focused on the biotic recovery following the ETME (Atkinson and Wignall, 2019). Here, we employ high-resolution pyrite framboid analysis (with sampling intervals generally < 0.5 m) of Tr-J boundary sections at Kuhjoch (Austria) and St. Audrie's Bay (England), generate data straddling the extinction interval, and compare these data with earlier studies (e.g., Wignall, 2001a), to evaluate the timing, duration and extent of marine anoxia in two palaeogeographically distant locations (Fig. 1). In doing so we provide further data about redox dynamics on the Tethyan shelf and thus evaluate the role of anoxia in the marine ETME through comparison with global records of anoxia.

2. Geological setting and background

The Kuhjoch section is located in the eponymous pass in the Karwendel Mountains, Northern Calcareous Alps, Austria (47°29'02"N, 11°31'50"E) (Fig.1) and is the Global Stratotype Section and Point for the Triassic-Jurassic boundary. The boundary is defined by the first occurrence of the ammonite *Psiloceras spelae* and the foraminifer *Praegubkinella turgescens* (Hillebrandt et al., 2013). Kuhjoch strata record deposition in the Eiberg Basin, an intra-platform trough adjacent to the Tethys Ocean. During the late Rhaetian, the Eiberg Basin attained estimated water depths of 150-200 m, rendering its benthic faunas somewhat immune to the effects of the well-documented end-Triassic eustatic sea-level fall (Hillebrandt et al., 2013). The stratigraphy includes the Triassic Kössen Formation (Eiberg Member) and the Triassic to Jurassic Kendlbach Formation (Tiefengraben and Breitenberg Members), with the Tr-J boundary placed 5.8 m above the base of this formation. The upper part of the Kössen Formation comprises a 20 cm-thick, dark coloured, marly limestone layer named the "T-bed" (Hillebrandt et al., 2007), interpreted to record oxygen-restricted deposition (Tanner et al., 2016). The T-bed marks the onset of the biotic crisis and is the level at which the last Triassic ammonoids, ostracods and conodonts disappeared. A prominent negative CIE (the initial CIE) occurs from the top of the T-bed into the lowermost Tiefengraben Member (Ruhl et al., 2009; Lindström et al., 2017). The Tiefengraben Member comprises grey-brown, clay-rich marls together with a 2 m thick red, silty clay horizon (known as the Schattwald Bed) near the base of the Formation. The Schattwald Bed is considered to record the peak of a latest Triassic regression (McRoberts et al., 2012). A second major negative $\delta^{13}C_{org}$ excursion (the main CIE) and palynological turnover occurs in the uppermost part of the Schattwald Bed (Hillebrandt et al., 2013). The paucity of macrofauna in the Schattwald Bed is suggested to be a function of the pervading unfavourable environment for calcifying organisms at the time of deposition (McRoberts et al., 2012) although this assertion is undermined by the occurrence of bivalves, foraminifers and uncommon ammonites and brachiopods at this level (Hillebrandt et al., 2013).

The St. Audrie's Bay section in southwest England (UK) is a former GSSP candidate for the base of Jurassic System (Warrington et al., 1994; Fig. 1). The strata include, from oldest to youngest, the Westbury, Lilstock and Blue Lias Formations. The Upper Triassic Westbury Formation comprises dark coloured, but not particularly organic-rich mudstones (mostly <2 wt.% total organic carbon; Hesselbo et al., 2004), with interbedded siltstones. Its depositional environment is interpreted as restricted marine with low salinity, based on a fossil content lacking stenohaline taxa (Hallam and

El Shaarawy, 1982; Hesselbo et al., 2004). The overlying Lilstock Formation (also Upper Triassic) is divided into two members: the Cotham Member and the Langport Member. The transition between the Westbury and Lilstock Formations is an upward-shallowing one, with the Cotham Member comprising mudstones, siltstones, limestones and fine-grained sandstones (calcareous in the upper part). The overlying Langport Member comprises marine limestones and calcareous mudstones (Hesselbo et al., 2004). A major negative carbon isotope excursion (the initial CIE) occurs in the Cotham Member a short distance above the level of a major extinction amongst the bivalves and ostracods that dominate the assemblages (Wignall and Atkinson, 2020). A second extinction phase occurs at the top of the Langport Member amongst the same two groups. The ETME can thus be resolved into two extinction phases at St. Audrie's Bay (a pattern seen elsewhere in the world), whereas at Kuhjoch only the first phase is clearly manifested (Wignall and Atkinson, 2020). The Blue Lias Formation of St. Audrie's Bay is characterized by rhythmic interbeds of laminated organic-rich shale, pale and dark marl and limestones that are interpreted to record rapid flooding (Hallam, 1997; Ruhl et al., 2010). The first appearance of typical Jurassic ammonites (*Psiloceras spelae*) that mark the Tr-J boundary occurs within this transgressive phase. However, Hodges (2021) suggested a lower placement of the Triassic-Jurassic boundary in SW Britain based on the discovery of *Neophyllites lavernockensis* in the topmost bed of the Langport Member; a level coincident with the second extinction level of Wignall and Atkinson (2020).

3. Material and methods

Pyrite framboids are densely packed, generally spherical aggregates of submicron-sized pyrite crystals. In the modern ocean, iron monosulfide (FeS) microcrysts nucleate in a reducing water mass before being replaced with greigite (Fe_3S_4) in weakly oxic environments, at which point they become densely packed spherical clusters (framboids). The greigite phase converts into the more stable pyrite (FeS_2) under reducing conditions during sediment burial. The majority of framboids in nature are formed near the redox boundary and their growth ceases in anoxic water columns beneath the sulfate-reduction zone (Wilkin et al., 1996). Framboids forming syngenetically within the sediment at the redox boundary (i.e., beneath an oxic water column) are larger than those forming within the water column in anoxic bottom waters because the growth of framboids within sediment is limited only by the availability of reactants. In modern euxinic basins, framboids sink into the sulfate-reduction zone and monosulfide microcrysts cease to form once they reach ~5 μm in diameter. In such settings, framboids can attain only small sizes (and are less variable in size, < 4% of framboids are >10 μm in diameter) than in non-euxinic settings (Wilkin et al., 1996). In modern dysoxic settings, around 10-50% of framboids in a population reach diameters >10 μm since pyrite framboids can continue growing on weakly oxygenated sediment surfaces where their size is limited only by the availability of reactants. Thus, dysoxic conditions are characterized by populations of relatively large framboids with a wide size distribution (Wilkin et al., 1996; Wignall and Newton, 1998).

In this study we analyzed framboidal pyrite size-frequency distributions for 35 samples from Kuhjoch and 43 samples from St. Audrie's Bay. Samples were prepared as vertically oriented thin sections (2×2 cm) before pyrite framboids were scanned and measured using an SU 8010 Scanning Electron Microscope (SEM) in the State Key Laboratory of Biogeology and Environmental Geology, Wuhan, China. We measured > 100 framboids per sample in order to account for the fact that the measured diameters of individual pyrite framboids are always equal to or smaller than their actual diameters. With this number of measurements, the error in the calculated mean of framboid diameters is < 10% (Wilkin et al., 1996). It is likely that very tiny framboids (e.g., 1-2 μm in diameter) are ignored or missed during the measuring process, inadvertently offsetting the error described above. Numerous studies have employed and refined the framboidal pyrite method in the past two decades such that it is has become a reliable, well-calibrated proxy for redox conditions during deposition of ancient sediments (Table 1).

Table 1. Characteristics of pyrite framboid populations formed under different marine redox conditions (from Bond and Wignall, 2010).

Redox conditions	**Framboidal parameters**
Euxinic	Small in size (mean 3-5 μm), abundant, with narrow size range. Framboids dominate pyrite fraction.
Anoxic	Small in size (mean 4-6 μm), abundant, with a few, lager framboids. Framboids dominate pyrite fraction.
Lower dysoxic	Mean 6-10 μm, moderately common, with a few, larger framboids and some crystalline pyrite.
Upper dysoxic	Moderately common to rare, broad range of sizes, only a small proportion <5 μm. Majority of pyrite as crystals.
Oxic	Very rare framboids, rare pyrite crystals.

4. Results

Of the 35 samples from Kuhjoch, 27 yielded framboids (Fig. 2) which contained a total of 2218 framboids, the size of each of was measured under SEM. Most samples contained >100 framboids (although framboids were rare in five samples). Samples with fewer than 20 framboids were excluded from our analysis. Pyrite framboids occur in both thin and thick units of both shale and limestone lithologies. The results are summarized in Appendix Table A and presented in Figure 2. The mean framboid diameters in individual samples ranges from 5.5 μm to 7.5 μm and all framboid diameters were < 20 μm.

Forty three thin sections were prepared for pyrite framboid analysis from St. Audrie's Bay. Of these, 40 samples contained a total of 2603 pyrite framboids and most samples contained >100 framboids. The pyrite framboid size-frequency data is summarized in Appendix Table B and presented in Figure 3. Mean framboid diameters range from 5 μm to 7.5 μm, with the exception of sample J2 (mean size: 9.57 μm). No framboid > 20 μm in diameter was observed in the St. Audrie's Bay samples.

The interpretation of water mass redox conditions from pyrite framboid size distributions is based on a combination of the mean of framboid diameters in each sample and the standard deviation within the population in each sample (Wilkin et al., 1996). This data is presented in Figure 4, which informs our interpretation of redox states in Figures 2 and 3.

5. Interpretation and discussion

5.1 Triassic-Jurassic marine redox conditions at Kuhjoch and St. Audrie's Bay

At Kuhjoch, the upper part of the Kössen Formation, including the T-Bed that saw the majority of ETME losses, was deposited under predominantly dysoxic or anoxic conditions (Figs. 2 and 4). Framboids also occur in the basal metres of the Kendlbach Formation, including some samples from the Schattwald Bed, although one sample from this level had only rare framboids (T-R+80 cm). Two samples from the Schattwald Bed contain framboids with size distributions characteristic of dysoxic (T-R+100 cm) and anoxic (T-R+2 m) conditions. It appears that anoxic-dysoxic conditions prevailed both before and during the ETME at Kuhjoch and then intermittently in the early stages of deposition of the Schattwald Bed within the Kendelbach Formation (Fig. 2). The presence of pyrite framboids in the Schattwald Bed is intriguing given that this unit is a red-coloured mudrock with a sparse marine fauna. Marine red beds are a rare phenomenon but in the Phanerozoic they are widespread in the aftermath of anoxic intervals (Song et al., 2017). They potentially owe their origin to the transition from euxinic to ferruginous conditions in the waning stages of anoxic events. The displacement of Fe^{2+}-rich waters into shallower settings produces sediments enriched with small ferric particles that impart the red color (Song et al. 2017). Adopting this model would imply that the Schattwald Beds formed upslope of a deeper, ferruginous water column, with both iron oxide precipitation and framboid growth occurring in the sediment.

At St. Audrie's Bay, pre-ETME samples from the Westbury Formation suggest that anoxic-euxinic conditions prevailed in the water column, with only one sample (S32) yielding a framboid population consistent with dysoxic conditions (Figs. 3 & 4). Two samples (S17 and S18) fall within the euxinic field whilst other samples fall within the anoxic field (Fig. 4). Samples from within the first phase of the ETME and near its base in Cotham Member (S12 to S16) show a narrow range of framboid size distributions (mean diameters between 5.99 and 6.71 μm), indicative of dysoxia or anoxia. The inferred redox levels are supported by iron speciation and molybdenum data from sediments at St. Audrie's Bay which also suggest anoxic to euxinic conditions developed at this level (He et al. 2022a), and by the persistence of high levels of isorenieratane (a marker for euxinia) from the Westbury Formation into the basal Cotham Member (Fox et al., 2022a). Shortly above the extinction level the framboid populations increase in size indicating a slight improvement in oxygenation although dysoxia is still inferred (Figs. 3,4). Wave ripples and a desiccation crack horizon occurs in the mid-Cotham Member suggesting that the dysoxic conditions were restricted to the sediment whilst the shallow waters were oxygenated.

Above the level of the first extinction pulse framboids suggest dysoxic conditions developed in the upper Cotham Member, before anoxic bottom waters returned in the Langport Member (note the basal metres, between sample S9 and S12, were not sampled for framboids). Iron speciation data suggest predominantly anoxic-ferruginous conditions for the entire Langport Member (He et al. 2022a). These interpretations are supported by the absence of isorenieratane (other than a single datum) which suggests euxinic conditions did not develop between the mid Cotham to top Langport level (Fox et al. 2022a). The uppermost part of the Cotham Member has generally been considered to be a non-marine succession based on its fossil content (Morton et al. 2017) and so the persistence of oxygen-restriction at this level is remarkable.

A thin black shale at the base of Blue Lias Formation, immediately above the level of the second extinction pulse, is known from various sections in SW England where it has been called the “paper shales”. Framboid populations from this bed at Pinhay Bay (ca. 60 km south of St. Audrie’s Bay; mean diameter: 4.52 μm, standard deviation: 1.54) are characteristic of euxinic conditions (Wignall, 2001a; Fig. 3). Euxinic conditions here are supported by more recent framboid (Atkinson and Wignall, 2019) and biomarker studies (Beith et al., 2021; Fox et al., 2022a). Oxygen-poor conditions persisted during deposition of the lower part of the Blue Lias Formation at St. Audrie’s Bay, although earliest Jurassic samples yield framboid populations with larger maximum framboid sizes (up to 19.9 μm) suggestive of dysoxia rather than anoxia (Figs. 3 & 4).

In summary, pyrite framboid size-frequency distributions indicate that oxygen-poor conditions were developed on the seafloor prior to the ETME at both Kuhjoch and St. Audrie’s Bay. Anoxia persisted after the first pulse of extinction when it spread even into very shallow waters. There were brief phases of more oxygenated conditions prior to a euxinic interval coincident with the second extinction pulse at St. Audrie’s Bay. The second pulse (of extinction and euxinia) is not seen at Kuhjoch, where oxygenation levels improve above the base of the Kendlbach Formation.

5.2 Other records of marine anoxia during the Triassic-Jurassic transition

The global extent and duration of anoxia and its link with extinction during the

Triassic-Jurassic transition is relatively poorly understood (e.g., Luo et al. 2018). Here we compare marine redox records across the ETME and Tr-J boundary for different regions of Panthalassa, Western Tethys and the Central European Basin (Fig. 5).

Isorenieratane, a biomarker for green sulfur bacteria, has been recorded from the Blue Lias Formation (Jaraula et al., 2013; Fox et al., 2022a) suggesting photic zone euxinia developed at, and immediately above the level of the second extinction pulse, as confirmed by our pyrite framboid analysis from St. Audrie's Bay. In contrast to the record of anoxia at St. Audrie’s Bay, our pyrite framboid analysis for Kuhjoch indicates that anoxic conditions were only developed around the level of the initial CIE and the main extinction losses, before bottom water oxygen levels increased leading initially to dysoxic conditions in the extinction aftermath and then to fully oxic conditions across the Tr-J boundary. This history is largely consistent with Pálfy and Zajzon’s (2012) elemental geochemistry study (U/Th ratio and Ce anomalies) of the nearby Kendlbach section which found no evidence for water column anoxia during the Tr-J transition.

In the north German locations, pyrite sulfur isotope analysis and biomarker data suggest that euxinic conditions became widespread during the earliest Jurassic, but that oxygen levels were normal during the extinction crisis which occurs at the level of the Triletes Bed (Richoz et al., 2012; Luo et al., 2018; Fig. 5). This is a laminated, organic-poor mudstone that is rich in trilete lycopod megaspores and also contains rare dinoflagellate cysts (van de Schootbrugge et al., 2009). The depositional environment of the Triletes Bed is enigmatic and merits further study, but it could record a shallow-water, restricted environment that was well oxygenated but of low salinity.

Elsewhere in western Tethys, a large, positive $\delta^{34}S_{CAS}$ excursion has been observed from the ETME interval in the Mount Sparagio section (Italy), prior to a return to background values before the Tr-J boundary. This is interpreted as evidence for globally enhanced pyrite burial under widespread and intensely anoxic conditions during the extinction interval (He et al., 2020). We note that the extinction level from He et al. (2020) is placed immediately below the Tr-J boundary as defined by the first occurrence of Jurassic taxa. The initial CIE at Mount Sparagio has been placed considerably lower in the section (Todaro et al. 2018), although the $\delta^{13}C_{carb}$ record shows many oscillations at this site including several negative excursions above the "initial CIE". Jost et al. (2017) identified a negative uranium isotope excursion that is indicative of anoxia during the ETME but with an intensification around the Tr-J boundary. However, Jost et al. (2017) placed the Tr-J boundary at the base of the Malanotte Formation, coincident with the initial negative CIE, a level generally taken to be within the latest Triassic. In contrast, Zaffani et al. (2018) placed the initial CIE in the Calcari Formation (the strata below the Malanotte Formation), a placement that seems to be more consistent with other records. The sulfur and uranium isotope records indicate increasingly oxygenated conditions in the Hettangian (Fig. 5).

Analyses of nitrogen isotopes and redox-sensitive trace metals (e.g., U and Mo) in the mid-Panthalassa Kurusu section of Japan indicate that bottom waters were generally well oxygenated in deep mid-Panthalassa through the Tr-J interval, although mid-water oxygen deficiency may have intensified at this time (Fujisaki et al., 2020). However, in the northeastern Panthalassan outer shelf / upper slope Kennecott Point section of western Canada, biomarkers suggest episodic PZE during and after the ETME interval and into the Jurassic (Kasprak et al., 2015). Nitrogen isotope and trace metals (U and Mo) at Kennecott Point indicate low nitrogen availability in an ocean with limited productivity and an expanded oxygen minimum zone (OMZ; Schoepfer et al., 2016). Low sulfate conditions might have promoted the expansion of marine anoxia during rapid warming events, as modelled by He et al., (2020). Large perturbations in the sulfur isotope record coincident with the onset of ETME have been detected at Kennecott Point (Willford et al., 2009) and the Black Bear Ridge section on the Canadian mainland (He et al., 2020), indicative of widespread marine anoxia in Panthalassa during a time of low oceanic sulfate concentrations.

A vertically expanded OMZ model has been suggested for the end-Triassic marine redox scenario (Fujisaki et al., 2020), and here we present a similar model (Fig. 6) in which anoxic water developed in shallow waters during the early stages of the ETME. Anoxia may also have developed in the not fully marine (lagoonal?) post-extinction interval of the upper Cotham Member, although potentially comparable facies of the Triletes Bed in Germany do not record anoxic deposition. A similar expansion of oxygen-poor conditions into exceptionally shallow waters has been recorded in the peritidal carbonates at Mount Sparagio (Sicily) in western Tethys based on a decline of I/(Ca + Mg) ratios at the time of extinction (He et al. 2022b).

While the size distribution of pyrite framboids in our study suggests that anoxic-dysoxic conditions were developed prior to the Tr-J extinction event at both Kuhjoch and St. Audrie’s Bay, oxygen-poor conditions are not well-documented prior to the

ETME in other stratigraphic sections from the Central European Basin (Fig.5). It is plausible that while some areas became inimical for life shortly before mass extinction, benthic taxa could flourish in more habitable zones elsewhere in Europe (i.e. within oxygenated refugia). Only with the spread of dysoxia/anoxia was an extinction crisis precipitated. The intensity and duration of marine anoxia/dysoxia during the ETME interval varies from location to location but there is a growing body of evidence for widespread oxygen-restriction at the extinction level (especially in the shallow water and photic zone). In the post-extinction aftermath, pyrite framboids measured in this study (St. Audrie's Bay) and by Atkinson and Wignall (2019) indicate that anoxic/dysoxic conditions persisted beyond the ETME in SW England. However, these oxygen-poor conditions do not appear to have delayed the biotic recovery after ETME. This suggests that, rather like in the case of our postulated pre-extinction refugia, well-oxygenated Early Jurassic sites (e.g., the Kuhjoch section) facilitated the biotic recovery (Atkinson and Wignall, 2019).

5.3 Drivers of marine anoxia during the Tr-J transition

Several mechanisms have been invoked as drivers of anoxia during the Mesozoic (e.g., Wignall, 2015; Reeshemius and Planavsky, 2021), including: A) elevated primary productivity; B) weakened ocean circulation, resulting in stratification, stagnation and anoxia; and C) ocean warming and a decline of dissolved oxygen. For the ETME, the expansion of the OMZ in Panthalassa suggests increased productivity, at least in this ocean. Enhanced continental weathering (associated with global warming) and increased nutrient flux is likely to have been a driver of these changes.

The CAMP is one of the most extensive and voluminous large igneous provinces known and it represents a plausible trigger for warming and ultimately marine anoxia at the end of the Triassic (Luo et al., 2018). Earliest CAMP activity predates the ETME interval (Davies et al., 2017), but the most intense volcanism coincided with the ETME (Schoene et al., 2010; Davis et al., 2017 and references therein). Large igneous provinces release large volumes of gases and volatiles, including water vapour, CO_2, SO_2, and halogens and their compounds (see reviews of Wignall, 2001b; Bond and Wignall, 2014; and Bond and Grasby, 2017). Model simulations have suggested that carbon and sulfur emissions could raise global temperature by 4.4 °C during a single pulse of CAMP activity (Landwehrs et al., 2020). In addition to volcanogenic volatiles, LIPs emplaced in organic-rich sedimentary basins are thought to generate large volume of thermogenic CO_2 and CH_4 during contact metamorphism of sediments surrounding sill intrusions (Svensen et al., 2004). Since CH_4 is highly depleted in ^{13}C, its release during contact metamorphism provides an explanation for the major negative CIEs around the ETME level (the initial CIE) and across the Tr-J boundary (the main CIE; Hesselbo et al., 2002). The extensive sills of the CAMP are estimated to have intruded a surface area of more than 10^6 km^2 of organic-rich sedimentary rocks and mature hydrocarbon-bearing strata making it likely that thermogenic greenhouse gases would have greatly contributed to an increase in atmospheric CO_2 (Lindström et al., 2021 and references therein). Potentially there is a role for dissociation of gas (methane) hydrates during the ETME (Hesselbo et al., 2002) has not been ruled out. However, the potency of gas hydrates in driving warming is questionable because hydrate melting is a self-limiting endothermic reaction. Furthermore, methane released in deep water is rapidly oxidized in the water column, greatly reducing its climatic effects (Ruppel, 2011).

The concentration of sedimentary mercury, normalized to total organic carbon (Hg/TOC), is an important proxy for volcanism during mass extinction crises (Sanei et al., 2012). The onset of positive Hg/TOC excursions in multiple Tr-J sections were likely driven by a single, early pulse of CAMP activity that was responsible for the initial CIE (Percival et al. 2017; Yager et al., 2021). At Kuhjoch, the development of anoxia inferred from pyrite framboids is broadly correlated to the onset of the rise in Hg/TOC at the beginning of the ETME (Fig. 6), and thus there is a likely a temporal, and probably a causal link between anoxia and the voluminous LIP volcanism of the CAMP.

6. Conclusions

Pyrite framboid analysis of samples from sections at St. Audrie’s Bay (England) and Kuhjoch (the Hettangian GSSP, Austria) reveal a varied redox history: the St. Audrie’s Bay record suggests that anoxic-euxinic conditions dominated the Tr-J interval, including both pulses of the ETME, and these conditions were only briefly interspersed with episodes of better oxygenated conditions. The development of oxygen-restriction in the extremely shallow waters of lower Cotham Member deposition would have greatly restricted marine habitat area and contributed substantially to the extinction losses. Pyrite framboids from Kuhjoch indicate a prevailing anoxic-dysoxic environment in the lead up to, and during, the main phase of ETME in the upper part of the Kössen Formation. These were replaced with generally better oxygenated conditions above the basal beds of the overlying Kendlbach Formation. The Tr-J boundary beds at Kuhjoch are well oxygenated, in contrast to the intense oxygen restriction seen at this level in other basins.

The intensity and duration of marine anoxia was variable across the Central European Basin, Western Tethys and Panthalassa but oxygen restriction was a consistent feature of the first phase of extinction in several locations. Widespread marine anoxia is therefore becoming a contender in the plethora of purported drivers of the ETME. The close temporal association of anoxia and Hg/TOC peaks supports a scenario in which large igneous province volcanism in the Central Atlantic Magmatic Province was the main driver of global climate change and marine oxygen depletion during the ETME.

Acknowledgements

We thank Hao Yang and Xincheng Qiu for their assistance during the analysis of pyrite framboids. This study was supported by National Natural Science Foundation of China (grant numbers: 42172032, 41872033, 41402302, and 41661134047). This is a contribution to International Geoscience Programme (IGCP) 630 “Permian and Triassic integrated Stratigraphy and Climatic, Environmental and Biotic Extremes.”

Appendix: framboidal pyrite data

Appendix table A. Framboidal pyrite data from the Kuhjoch section, Austria.

Sample	Height /m	n	Mean size/µm	Min	Max	Standard deviation	Redox conditions
T-R+9 m	13.1	5	9.6	7.5	14.4	*	dysoxic-oxic
T-R+8.6 m	12.7	59	7.4	3.4	14.3	2.3	dysoxic
T-R+7.8 m	11.9	18	13.0	9.2	17.2	2.5	dysoxic-oxic
T-R+5.6 m	9.7	1	*	*	*	*	
T-R+4 m	8.1	104	6.3	3.2	10.9	1.5	anoxic
T-R+2 m	6.1	106	7.0	2.8	11.7	1.9	anoxic
T-R+100 cm	5.1	108	7.3	3.4	19.4	2.5	dysoxic
T-R+80 cm	4.9	16	10.3	5.7	16.3	3.2	dysoxic-oxic
T-R+20 cm	4.3	*	*	*	*	*	
T-B-5	4.0	100	6.7	3.1	16.2	2.2	anoxic
T-B-4	3.9	108	5.9	1.4	11.9	1.7	anoxic
T-B+20 cm	3.5	*	*	*	*	*	
T-B+15 cm	3.45	107	6.7	2.5	15.6	2.4	dysoxic
T-B+5 cm	3.35	106	7.4	2.9	18.8	2.4	dysoxic
T-0	3.3	74	6.3	12.1	2.7	1.6	anoxic
T-10	3.2	100	6.8	3.2	14.8	2.1	dysoxic
T-20	3.1	98	7.0	2.4	19.0	2.5	dysoxic
T-40	2.9	98	6.7	3.3	18.5	2.2	dysoxic
T-55	2.75	59	7.0	2.7	16.3	2.1	dysoxic
T-85	2.45	104	6.2	2.3	19.0	2.6	dysoxic
T-100	2.3	100	6.6	3.1	19.4	2.6	dysoxic
T-120	2.1	107	6.3	3.1	17.7	2.1	dysoxic
T-130	2.0	104	6.1	3.8	10.9	1.3	anoxic
T-140	1.9	92	7.4	3.9	10.6	1.6	anoxic
T-150	1.8	20	7.4	5.1	11.4	1.7	dysoxic
T-180	1.5	107	6.5	2.7	15.9	2.2	dysoxic
T-190	1.4	101	5.8	2.4	15.9	2.4	anoxic
T-260	0.7	*	*	*	*	*	
T-310	0.2	106	7.0	3.5	17.6	2.2	dysoxic
T-330	0.0	110	6.4	2.0	12.1	1.8	anoxic

*stands for no, or only rarely observed pyrite framboids.

Appendix table B. Framboidal pyrite data from the St. Audrie's Bay section, England.

Sample	**Height /m**	**n**	**Mean size/μm**	**Min**	**Max**	**Standard deviation**	**Redox conditions**
J16	20.1	105	7.5	4.3	10.8	1.5	dysoxic
J15	19.5	44	7.0	3.7	12.1	2.0	dysoxic
J14	19.0	53	8.9	4.6	19.5	3.2	dysoxic
J13	18.7	*	*	*	*	*	
J12	18.4	127	6.0	2.3	12.9	2.0	anoxic
J11	17.9	55	6.8	3.9	14.7	2.3	dysoxic
J10	17.5	13	6.6	4.6	8.6	1.1	dysoxic
J9	17.0	*	*	*	*	*	
J8	16.6	100	5.8	2.9	10.6	1.6	anoxic
J7	16.1	119	5.6	2.7	14.5	2.0	anoxic
J6	15.7	127	5.8	2.3	14.0	1.9	anoxic
J5	15.4	57	6.2	2.1	13.4	2.1	dysoxic
J4	15.1	103	5.3	1.9	10.0	1.7	anoxic
J3	14.8	52	6.8	3.1	12.8	1.9	dysoxic
J2	14.3	81	9.6	2.7	18.6	4.1	dysoxic
J1	14.0	143	5.1	1.8	11.6	1.8	anoxic
T1	13.7	64	7.5	3.4	16.8	2.6	dysoxic
T2	13.4	50	6.2	2.9	16.9	2.4	dysoxic
T4	13.1	119	6.8	2.7	17.9	3.0	dysoxic
T5	12.7	101	5.6	2.7	11.6	1.6	anoxic
T6	12.4	102	6.8	2.5	19.9	2.9	dysoxic
T7	12.1	114	5.9	2.3	11.1	1.7	anoxic
T8	11.7	107	6.9	3.0	17.3	2.7	dysoxic
T9	11.4	99	5.9	3.4	12.9	1.7	anoxic
T10	10.9	114	7.0	3.5	19.2	2.5	dysoxic
T11	10.4	101	5.8	2.7	13.7	2.1	anoxic
S-3	9.8	121	6.2	3.2	17.1	1.9	anoxic
S-4	9.0	102	6.1	3.2	12.0	1.9	anoxic
S-6	8.4	149	7.1	3.2	14.3	1.5	anoxic
S-8	7.8	108	6.4	3.3	13.5	1.9	anoxic
S-9	7.5	126	5.7	3.0	10.7	1.3	anoxic
S-12	6.6	107	6.1	3.4	14.5	1.6	anoxic
S-14	6.1	130	6.7	3.5	14.8	1.9	anoxic
S-15	5.8	105	6.4	3.3	15.2	2.5	dysoxic
S-16	5.5	99	6.0	3.1	10.9	1.6	anoxic
S-17	5.2	103	4.4	2.5	9.9	1.3	euxinic

S-18	4.9	97	4.8	2.6	11.7	1.4	euxinic
S-22	3.6	120	5.8	3.0	10.8	1.8	anoxic
S-24	3.0	100	6.9	3.3	13.1	2.0	anoxic
S-32	0.6	49	7.5	4.0	17.6	2.7	dysoxic
S-33	0.3	101	5.5	2.4	12.7	1.8	anoxic

*stands for no, or only rarely observed pyrite framboids.

References cited

Atkinson, J.W., Wignall, P.B., 2019. How quick was marine recovery after the end-Triassic mass extinction and what role did anoxia play? Palaeogeog. Palaeoclim. Palaeoecol. 528, 99-119.

Beith, S.J., Fox, C.P., Marshall, J.E.A, Whiteside, J.H., 2021. Recurring photic zone euxinia in the northwest Tethys impinged end-Triassic extinction recovery. Palaeogeog. Palaeoclim. Palaeoecol. 584: 110680.

Beerling, D.J., Berner, R.A., 2002. Biogeochemical constraints on the Triassic-Jurassic boundary carbon cycle event. Glob. Biogeochem. Cycles 2002, 16(3), 10-1-10-13.

Belcher, C.M., Mander, L., Rein, G., Jervis, F.X., Haworth, M., Hesselbo, S.P., Glasspool, I.J., McElwain, J.C., 2010. Increased fire activity at the Triassic/Jurassic boundary in Greenland due to climate-driven floral change. Nat. Geosci. 3(6): 426-429.

Bond, A.D., Dickson, A.J., Ruhl, M., Raine, R., 2022. Marine redox change and extinction in Triassic–Jurassic boundary strata from the Larne Basin, Northern Ireland. Palaeogeog. Palaeoclim. Palaeoecol. 598: 111018.

Bond, D.P.G., Wignall, P.B., 2010. Pyrite framboid study of marine Permian–Triassic boundary sections: A complex anoxic event and its relationship to contemporaneous mass extinction. Geol. Soc. Am. Bull. 122(7-8), 1265-1279.

Bond, D.P.G., Wignall, P.B., 2014. Large igneous provinces and mass extinctions: an update. Volcanism, impacts, and mass extinctions: causes and effects, 505, p. 29-55.

Bond, D.P.G., Grasby, S.E., 2017. On the causes of mass extinctions. Palaeogeog. Palaeoclim. Palaeoecol. 478, 3-29.

Bonis, N.R., Ruhl, M., Kürschner, W.M., 2010a. Climate change driven black shale deposition during the end-Triassic in the western Tethys. Palaeogeog. Palaeoclim. Palaeoecol. 290(1-4), 151-159.

Bonis, N.R., Van Konijnenburg-Van Cittert, J.H.A., Kürschner, W.M., 2010b. Changing CO2 conditions during the end-Triassic inferred from stomatal frequency analysis on Lepidopteris ottonis (Goeppert) Schimper and Ginkgoites taeniatus (Braun) Harris. Palaeogeog. Palaeoclim. Palaeoecol. 295(1-2), 146-161.

Dai, X., Song, H.J., Wignall, P.B., Jia, E.H., Bai, R.Y., Wang, F.Y., Chen, J., Tian, L., 2018. Rapid biotic rebound during the late Griesbachian indicates heterogeneous recovery patterns after the Permian-Triassic mass extinction. Geol. Soc. Am. Bull. 130 (11-12), 2015–2030.

Davies, J.H.F.L., Marzoli, A., Bertrand, H., Youbi, N., Ernesto, M., Schaltegger, U., 2017. End-Triassic mass extinction started by intrusive CAMP activity. Nat. Commun. 8(1), 1-8.

Fox, C.P., Whiteside, J.H., Olsen, P.E., Cui, X.Q., Summons, R.E., Idiz, E., Grice, K., 2022a. Two-pronged kill mechanism at the end-Triassic mass extinction. Geology, 50(4), 448-453.

Fox, C.P., Whiteside, J.H., Olsen, P.E., Grice, K., 2022b. Flame out! End-Triassic mass extinction polycyclic aromatic hydrocarbons reflect more than just fire. Earth Planet. Sci. Lett. 584, 117418.

Fujisaki, W., Fukami, Y., Matsui, Y., Sato, T., Sawaki, Y., Suzuki, K., 2020. Redox conditions and nitrogen cycling during the Triassic-Jurassic transition: A new perspective from the mid-Panthalassa. Earth-Sci. Rev. 204, 103173.

Greene, S.E., Martindale, R.C., Ritterbush, K.A., Bottjer, D.J., Corsetti, F.A., Berelson, W.M., 2012. Recognising ocean acidification in deep time: An evaluation of the evidence for acidification across the Triassic-Jurassic boundary. Earth-Sci. Rev. 113(1-2), 72-93.

Guex, J., Bartolini, A., Atudorei, V., Taylor, D., 2004. High-resolution ammonite and carbon isotope stratigraphy across the Triassic–Jurassic boundary at New York Canyon (Nevada). Earth Planet. Sci. Lett. 225(1-2), 29-41.

Hallam, A., El Shaarawy, Z., 1982. Salinity reduction of the end-Triassic sea from the Alpine region into northwestern Europe. Lethaia 15(2), 169-178.

Hallam, A., 1997. Estimates of the amount and rate of sea-level change across the Rhaetian-Hettangian and Pliensbachian-Toarcian boundaries (latest Triassic to earliest Jurassic). J. Geol. Soc. 154(5), 773-779.

Hallam, A., Wignall, P.B., 1997. Mass Extinctions and Their Aftermath. Oxford, Oxford University Press, UK, 320 p.

Hautmann, M., 2004. Effect of end-Triassic CO2 maximum on carbonate sedimentation and marine mass extinction. Facies 50(2), 257-261.

He, T.C., Dal Corso, J., Newton, R.J., Wignall, P.B., Mills, B.J.W., Todaro, S., Stefano, P.D., Turner, E.C., Jamieson, R.A., Randazzo, V., Rigo, M., Jones, R.E., Dunhill, A.M., 2020. An enormous sulfur isotope excursion indicates marine anoxia during the end-Triassic mass extinction. Sci. Adv. 6(37), eabb6704.

He, T.C., Wignall, P.B., Newton, R.J., Atkinson, J.W., Keeling, J.F.J., Xiong, Y.J., Poulton, S.W., 2022a. Extensive marine anoxia in the European epicontinental sea during the end-Triassic mass extinction. Glob. Planet. Change 210, 103771.

He, T.C., Newton, R.J., Wignall, P.B., Reid, S., Dal Corso, J., Takahashi, S., Wu, H.P., Todaro, S., Stefano, P.D., Randazzo, V., Rigo, M., Dunhill, A.M., 2022b. Shallow ocean oxygen decline during the end-Triassic mass extinction. Glob. Planet. Change 210, 103770.

Hesselbo, S.P., Robinson, S.A., Surlyk, F., Piasecki, S., 2002. Terrestrial and marine extinction at the Triassic-Jurassic boundary synchronized with major carbon-cycle perturbation: A link to initiation of massive volcanism? Geology 30(3), 251-254.

Hesselbo, S.P., Robinson, S.A., Surlyk, F., 2004. Sea-level change and facies development across potential Triassic–Jurassic boundary horizons, SW Britain. J. Geol. Soc. 161(3), 365-379.

Hillebrandt, A.V., Kürschner, W.M, Krystyn, L., 2007. A candidate GSSP for the base of the Jurassic in the Northern Calcareous Alps (Kuhjoch section, Karwendel mountains, Tyrol, Austria). International Subcommission on Jurassic Stratigraphy Newsletter, 34(1), 2-20.

Hillebrandt, A.V., Krystyn L., Kürschner W.M. Bonis, N.R., Ruhl, M., Richoz, S., Schobben, M. A.N., Urlichs, M., Bown, P.R., Kment, K., McRoberts, C.A., Simms, M., and Tomãsových, A., 2013. The Global Stratotype Sections and Point (GSSP) for the base of the Jurassic System at Kuhjoch (Karwendel Mountains, Northern Calcareous Alps, Tyrol, Austria). Episodes 36(3), 162-198.

Hodges, P., 2021. A new ammonite from the Penarth Group, South Wales and the base of the Jurassic System in SW Britain. Geological Magazine 158(6), 1109-1114.

Huang Y.G., Chen Z.Q., Algeo T.J., Zhao, L., Aymon, B., Bhat, G., Zhang, L., Guo, Z., 2019. Two-stage marine anoxia and biotic response during the Permian–Triassic transition in Kashmir, northern India: pyrite framboid evidence. Glob. Planet. Change 172, 124-139.

Jaraula, C.M.B, Grice, K., Twitchett, R.J., Böttcher, M.E., LeMetayer, P., Dastidar, A.G., Opazo, L.F., 2013. Elevated pCO2 leading to Late Triassic extinction, persistent photic zone euxinia, and rising sea levels. Geology 41(9), 955-958.

Jost, A.B., Bachan, A., van de Schootbrugge, B., Lau, K.V., Weaver, K.L., Mahl, K., Payne, J.L., 2017. Uranium isotope evidence for an expansion of marine anoxia during the end-Triassic extinction. Geochem. Geophys. Geosyst. 18(8), 3093-3108.

Kaiho, K., Tanaka, D., Richoz, S., Jones, D.S., Saito, R., Kameyama, D., Ikeda, M., Takahashi, S., Md. Aftabuzzaman, Fujibayashi, M., 2022. Volcanic temperature changes modulated volatile release and climate fluctuations at the end-Triassic mass extinction. Earth Planet. Sci. Lett. 579, 117364.

Kasprak, A.H., Sepúlveda J, Price-Waldman, R., Williford, K.H., Schoepfer, S.D., Haggart, J.W., Ward, P.D., Summons, R.E., Whiteside, J.H., 2015. Episodic photic zone euxinia in the northeastern Panthalassic Ocean during the end-Triassic extinction. Geology 43(4), 307–310.

Kiessling W, Aberhan M, Brenneis B, Wagner, P., 2007. Extinction trajectories of benthic organisms across the Triassic-Jurassic boundary. Palaeogeog. Palaeoclim. Palaeoecol. 244(1-4), 201-222.

Kovács, E.B, Ruhl, M., Demény, A., Fórizs, I., Hegyi, I., Horváth-Kostka, Z.R., Móriczg, F., Vallnera, Z., Pálfy, J., 2020. Mercury anomalies and carbon isotope excursions in the western Tethyan Csővár section support the link between CAMP volcanism and the end-Triassic extinction. Glob. Planet. Change 194, 103291.

Kump, L.R., Arthur, M.A., 1999. Interpreting carbon-isotope excursions: Carbonates and organic matter. Chem. Geol. 161(1-3), 181-198.

Landwehrs, J.P., Feulner, G., Hofmann, M., Petri. S., 2020. Climatic fluctuations modeled for carbon and sulfur emissions from end-Triassic volcanism. Earth Planet. Sci. Lett. 537, 116174.

Lindström, S., Van De Schootbrugge, B., Hansen, K.H., Pedersen, G.K., Alsen, P., Thibault, N., Dybkjær, K., Nielsen., L.H., 2017. A new correlation of Triassic–Jurassic boundary successions in NW Europe, Nevada and Peru, and the Central Atlantic Magmatic Province: a time-line for the end-Triassic mass extinction. Palaeogeog. Palaeoclim. Palaeoecol. 478, 80-102.

Lindström, S., Sanei, H., Van De Schootbrugge, B., Pedersen, G.K., Lesher, C.E., Tegner, C., Heunisch, C., Dybkjær, K., Outridge, P.M., 2019. Volcanic mercury and mutagenesis in land plants during the end-Triassic mass extinction. Sci. Adv. 5(10): eaaw4018.

Lindström, S., Callegaro, S., Davies, J., Tegner, C., Van De Schootbrugge, B., Pedersen, G.K., Youbi, N., Sanei, H., Marzoli, A., 2021. Tracing volcanic emissions from the Central Atlantic Magmatic Province in the sedimentary record. Earth-Sci. Rev. 212, 103444.

Luo, G.M., Richoz, S., Van De Schootbrugge, B., Algeo T.J., Xie, S., Ono, S., Summons, R.E., 2018. Multiple sulfur-isotopic evidence for a shallowly stratified ocean following the Triassic-Jurassic boundary mass extinction. Geochim. Cosmochim. Acta 231, 73-87.

Marynowski, L. Simoneit, B.R.T., 2009. Widespread Upper Triassic to Lower Jurassic wildfire records from Poland: evidence from charcoal and pyrolytic polycyclic aromatic hydrocarbons. Palaios 24(12): 785-798.

McElwain, J.C., Beerling, D.J., Woodward, F.L., 1999. Fossil plants and global warming at the Triassic-Jurassic boundary. Science 285(5432), 1386-1390.

McRoberts, C.A., Krystyn, L., Hautmann, M., 2012. Macrofossil response to the end-Triassic mass extinction in the West-Tethyan Kössen Basin, Austria. Palaios 27(9), 607-616.

Morton, J.D., Whiteside, D.I., Hethke, M., Benton, M.J. 2017. Biostratigraphy and geometric morphometrics of conchostracans (Crustacea, Branchiopoda) from the Late Triassic fissure deposits of Cromhall Quarry, UK. Palaeontology 60, 349-374.

Olsen, P.E., Kent, D.V., Sues, H.D., Koeberl, C., Huber, H., Montanari, A., Rainforth, E.C., Fowell, S.J., Szajna, M.J., Hartline, B. W. 2002. Ascent of dinosaurs linked to an iridium anomaly at the Triassic-Jurassic boundary. Science 296(5571), 1305-1307.

Pálfy, J., Mortensen, J.K., Carter, E.S., Smith P.L., Friedman, R.M., Tipper, H.W., 2000. Timing the End-Triassic mass extinction: First on land, then in the sea? Geology 28(1), 39–42.

Pálfy, J., Zajzon, N., 2012. Environmental changes across the Triassic– Jurassic boundary and coeval volcanism inferred from elemental geochemistry and mineralogy in the Kendlbachgraben section (Northern Calcareous Alps, Austria). Earth Planet. Sci. Lett. 335, 121-134.

Percival, L.M.E., Ruhl, M., Hesselbo S.P., Jenkyns, H.C., Mather, T.A., Whiteside, J.H., 2017. Mercury evidence for pulsed volcanism during the end-Triassic mass extinction. Proc. Natl. Acad. Sci. 114(30), 7929-7934.

Reershemius, T., Planavsky, N.J., 2021. What controls the duration and intensity of ocean anoxic events in the Paleozoic and the Mesozoic?. Earth-Sci. Rev. 221, 103787.

Petersen, H.I., Lindström, S., 2012. Synchronous wildfire activity rise and mire deforestation at the Triassic–Jurassic boundary. PLoS One 7, e47236.

Richoz, S., Van De Schootbrugge, B., Pross, J., Püttmann, W., Quan, T.M., Lindström, S., Heunish, C., Fiebig, J., Maquil, R., Schouten, S., Hauzenberger, C.A. & Wignall, P. B., 2012. Hydrogen sulphide poisoning of shallow seas following the end-Triassic extinction. Nat. Geosci. 5(9), 662-667.

Ruhl, M., Kürschner, W.M., Krystyn, L., 2009, Triassic-Jurassic organic carbon isotope stratigraphy of key sections in the western Tethys realm (Austria). Earth Planet. Sci. Lett. 281(3-4), 169–187.

Ruhl, M., Veld, H., Kürschner, W.M., 2010. Sedimentary organic matter characterization of the Triassic–Jurassic boundary GSSP at Kuhjoch (Austria). Earth Planet. Sci. Lett. 2010, 292(1-2), 17-26.

Ruhl, M., Bonis, N.R., Reichart, G.J., Sinninghe Damsté, J.S., Kürschner, W.M., 2011. Atmospheric carbon injection linked to end-Triassic mass extinction. Science 2011, 333(6041), 430-434.

Ruppel, C.D., 2011. Methane hydrates and contemporary climate change. Nature Eduction Knowledge, 2(12), 12.

Sanei, H., Grasby, S.E., Beauchamp, B., 2012. Latest Permian mercury anomalies. Geology 40(1), 63–66.

Schoene, B., Guex, J., Bartolini, A., Schaltegger, U., Blackburn, T. J., 2010. Correlating the end-Triassic mass extinction and flood basalt volcanism at the 100 ka level. Geology 38(5), 387–390.

Schoepfer, S.D., Algeo, T.J., Ward, P.D., Williford, K.H., Haggart, J.W., 2016. Testing the limits in a greenhouse ocean: did low nitrogen availability limit marine productivity during the end-Triassic mass extinction? Earth Planet. Sci. Lett. 451, 138–148.

Song, H.J., Jiang, G.Q., Poulton, S.W., Wignall, P.B., Tong, J.N., Song, H.Y., An, Z.H., Chu, D.L., Tian, L., She, Z.B., & Wang, C.S., 2017. The onset of widespread marine red beds and the evolution of ferruginous oceans. Nat. Commun. 8(1), 1-7.

Song, H.J., Wignall, P.B., Dunhill, A.M., 2018. Decoupled taxonomic and ecological recoveries from the Permo-Triassic extinction. Sci. Adv. 4(10), eaat5091.

Song, H.J., Kemp, D.B., Tian, L., Chu, D.L., Song, H.Y., Dai, X., 2021. Thresholds of temperature change for mass extinctions. Nat. Commun. 12(1), 1-8.

Steinthorsdottir, M., Jeram, A.J., McElwain, J.C., 2011. Extremely elevated CO2 concentrations at the Triassic/Jurassic boundary. Palaeogeog. Palaeoclim. Palaeoecol. 308(3-4), 418–432.

Svensen, H., Planke, S., Malthe-Sorenssen, A., Jamtveit, B., Myklebust, R., Eidem, T.R., Rey, S.S., 2004. Release of methane from a volcanic basin as a mechanism for initial Eocene global warming. Nature 429(6991), 542-545.

Tanner, L.H., Kyte, F.T., Richoz, S., Krystyn, L., 2016. Distribution of iridium and associated geochemistry across the Triassic–Jurassic boundary in sections at Kuhjoch and Kendlbach, Northern Calcareous Alps, Austria. Palaeogeog. Palaeoclim. Palaeoecol. 449, 13–26.

Thibodeau, A.M., Ritterbush, K., Yager, J.A., West, A.J., Ibarra, Y., Bottjer, D.J., Berelson, W.M., Bergquist, B.A., Corsetti F.A., 2016. Mercury anomalies and the timing of biotic recovery following the end-Triassic mass extinction. Nat. Commun. 7(1), 1-8.

Todaro, S., Rigo, M., Randazzo, V., Di Stefano, P., 2018. The end-Triassic mass extinction: A new correlation between extinction events and δ13C fluctuations from a Triassic-Jurassic peritidal succession in western Sicily. Sediment. Geol.

368: 105-113.

Van de Schootbrugge, B., Quan, T.M., Lindström, S., Puttmann, W., Heunisch, C., Pross, J., Fiebig, J., Petschick, R., Röhling, H.-G., Richoz, S., Rosenthal, Y., Falkowski, P.G. 2009. Floral changes across the Triassic/Jurassic boundary linked to flood basalt volcanism. Nat. Geosci. 2(8), 589-594. Doi:10.1038/NGE0577.

Van de Schootbrugge, B., Van Der Weijst, C.M.H., Hollaar, T.P., Vecoli, M., Strother, P. K., Kuhlmann, N., Thein, J., Visscher, H., van Konijnenburg-van Cittert, H., Schobben, M. A. N., Sluijs, A., Lindström, S., 2020. Catastrophic soil loss associated with end-Triassic deforestation. Earth-Sci. Rev. 210: 103332.

Warrington, G., Cope, J.C.W., Ivimey-Cook, H.C., 1994. St Audrie's Bay, Somerset, England: a candidate global stratotype section and point for the base of the Jurassic system. Geological Magazine. 131(2): 191-200.

Wignall, P.B., Newton, R.J., 1998. Pyrite framboid diameter as a measure of oxygen deficiency in ancient mudrocks. Amer. J. Sci. 298(7), 537-552.

Wignall, P.B., 2001a. Sedimentology of the Triassic-Jurassic boundary beds in Pinhay Bay (Devon, SW England). Proc. Geol. Assoc. 112(4), 349-360.

Wignall, P.B., 2001b. Large igneous provinces and mass extinctions. Earth-Sci. Rev. 53(1-2), 1-33.

Wignall, P.B., Zonneveld, J.-P., Newton, R.J., Amor, K., Sephton, M.A. Hartley, S., 2007. The end Triassic mass extinction record of Williston Lake, British Columbia. Palaeogeog. Palaeoclimat. Palaeoecol. 253, 385-406.

Wignall, P.B., Bond, D.P.G., Kiyoko, K., Kakuwa, Y., Newton, R.J., Poulton., S.W.,

2010. An 80 million year oceanic redox history from Permian to Jurassic pelagic sediments of the Mino-Tamba terrane, SW Japan, and the origin of four mass extinctions. Glob. Planet. Change 71(1-2), 109-123.

Wignall, P.B., 2015. The worst of times: how life on Earth survived eighty million years of extinctions. Princeton Univ. Press, 199 pp.

Wignall, P.B., Atkinson, J.W., 2020. A two-phase end-Triassic mass extinction. Earth-Sci. Rev. 208, 103282.

Wilkin, R.T., Barnes, H.L., Brantley, S.L., 1996. The size distribution of framboidal pyrite in modern sediments: An indicator of redox conditions. Geochim. Cosmochim. Acta 60(20), 3897-3912.

Williford H., Foriel, J., Ward, P.D., Steig, E.J., 2009. Major perturbation in sulfur cycling at the Triassic-Jurassic boundary. Geology 37(9), 835-838.

Yager, J.A., West, A.J., Thibodeau, A.M., Corsetti, F.A., Rigo, M., Berelson, William M., Bottjer, D.J., Greene, S.E., Ibarra, Y., Jadoul, F., Ritterbush, K.A., Rollins, N., Rosas, S., Di Stefano, P., Sulca, D., Todaro, S., Wynn, P., Zimmermann, L., Bergquist, B.A., 2021. Mercury contents and isotope ratios from diverse depositional environments across the Triassic–Jurassic Boundary: Towards a more robust mercury proxy for large igneous province magmatism[J]. Earth-Sci. Rev. 223: 103775.

Zaffani, M., Jadoul, F., Rigo, M., 2018. A new Rhaetian δ13Corg record: carbon cycle disturbances, volcanism, End-Triassic mass Extinction (ETE). Earth-Sci. Rev. 178: 92-104.

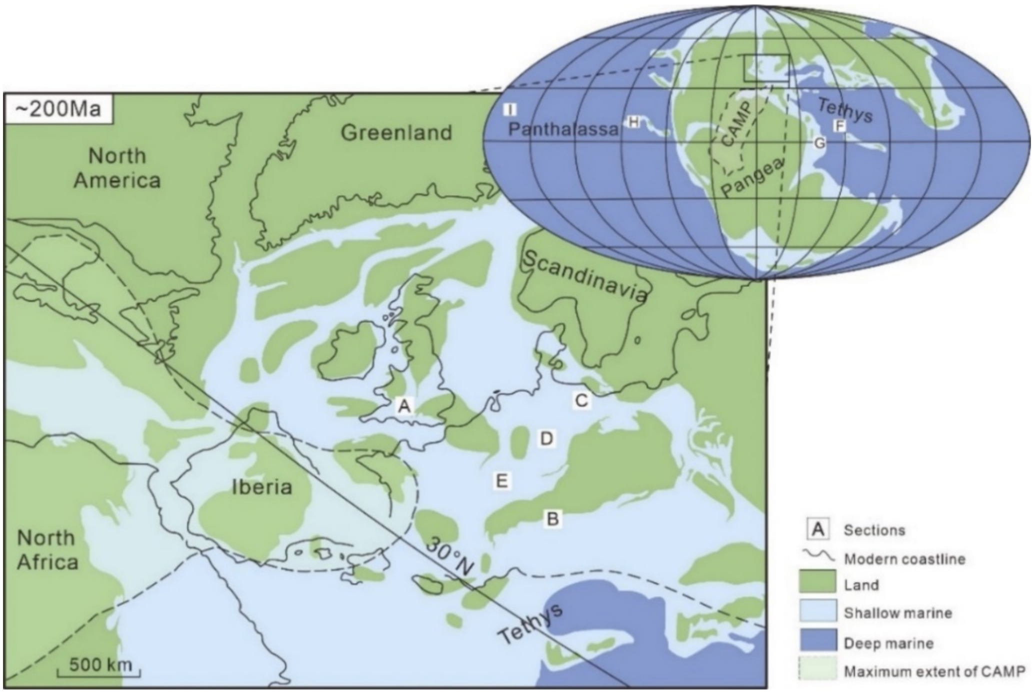

Fig. 1. Palaeogeographic map of the world and Europe across the Triassic-Jurassic boundary (adapted from Greene et al. (2012) and Lindström et al. (2017)). The dotted area represents the maximum geographic extent of the CAMP. Sections mentioned in the text: A. St. Audrie's Bay, UK (study section); B. Kuhjoch, Austria (study section); C. Mariental, Germany; D. Minglesheim, Germany; E. Rosswinkel FR 204-201 core, Luxemburg; F. Lombardy Basin, Italy; G. Mount Sparagio, Italy; and on the world map H. Kennecott Point, Canada; I. Kurusu, Japan.

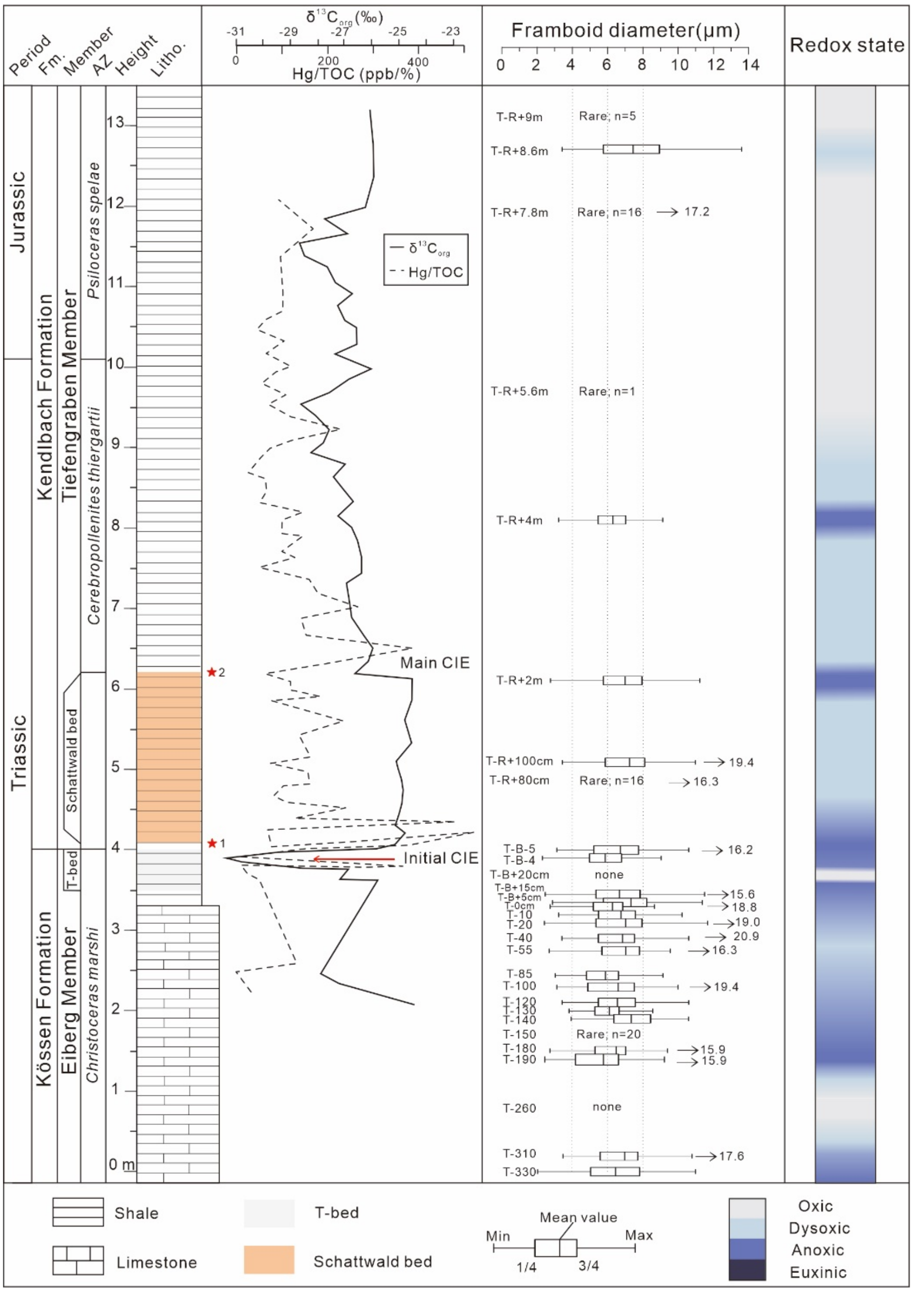

Fig. 2. Log of the Kuhjoch Tr-J succession including pyrite framboid ‘box-and-whisker’ plots and inferred redox states. δ^{13}C$_{org}$ data are from Ruhl et al. (2009) and the Hg/TOC data is from Percival et al. (2017). The ‘box’ depicts the 25th and 75th percentile of framboid size distributions, the ‘whiskers’ depict the minimum and maximum framboid diameters, and the central line records the mean framboid diameter. Fm. = Formation; AZ = Ammonite zone; Litho. = Lithology. Stars 1 and 2 are the levels of two extinction pulses based on Wignall and Atkinson (2020), though the second pulse is poorly defined at Kuhjoch.

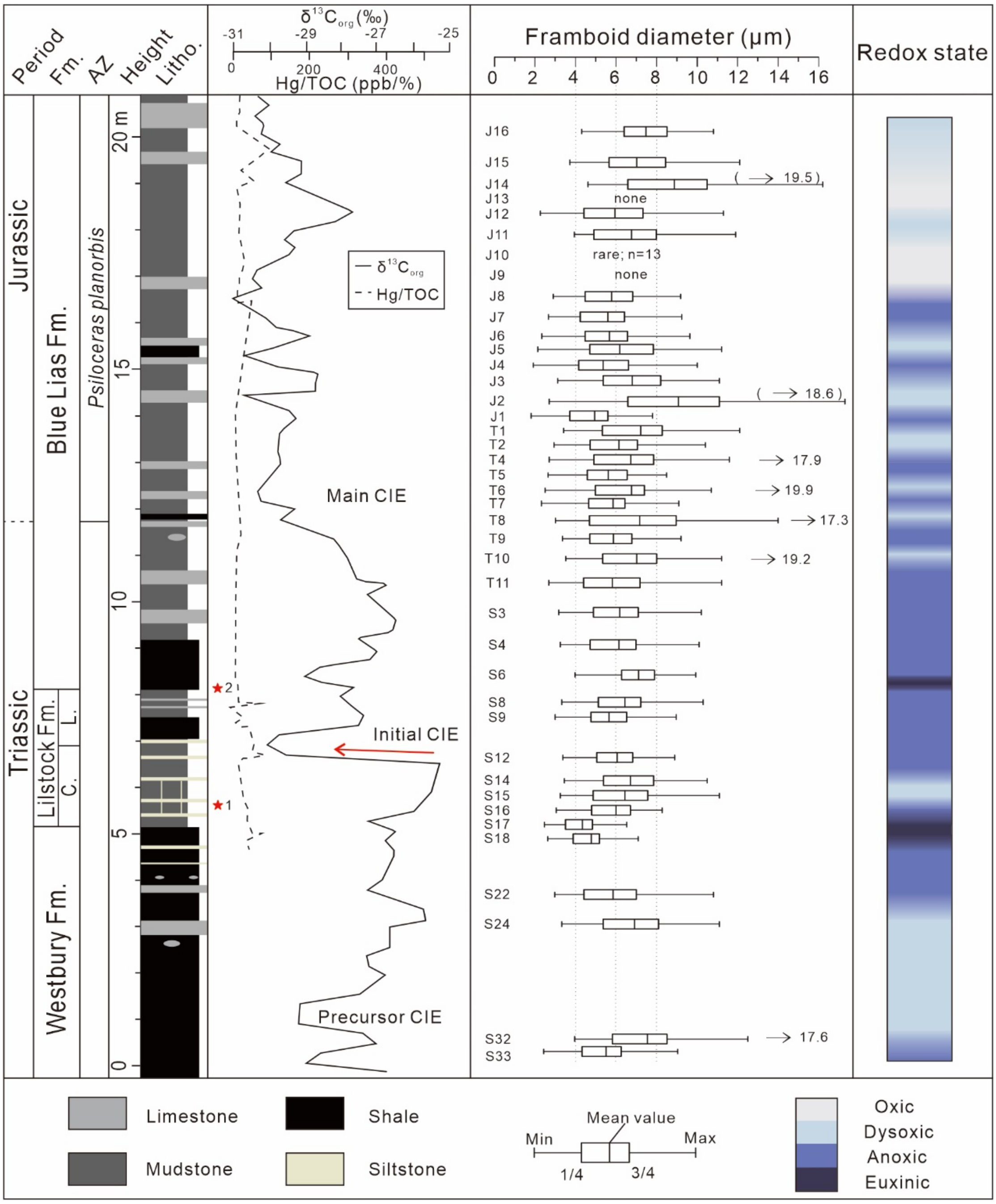

Fig. 3. Log of the St. Audrie's Bay Tr-J succession including pyrite framboid 'box-and-whisker' plots and inferred redox states. Δ^{13}C$_{org}$ data are from Hesselbo et al., 2002, and the Hg/TOC data is from Percival et al. (2017). C = Cotham Member; L = Langport Member.

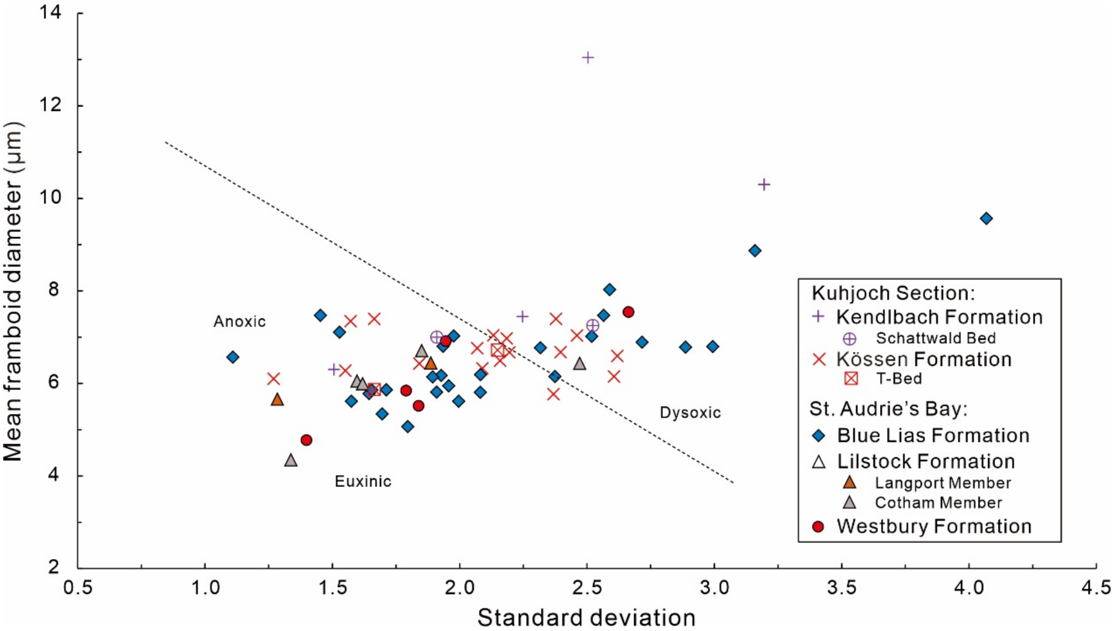

Fig. 4. Scatterplot of mean framboid diameter and standard deviation.

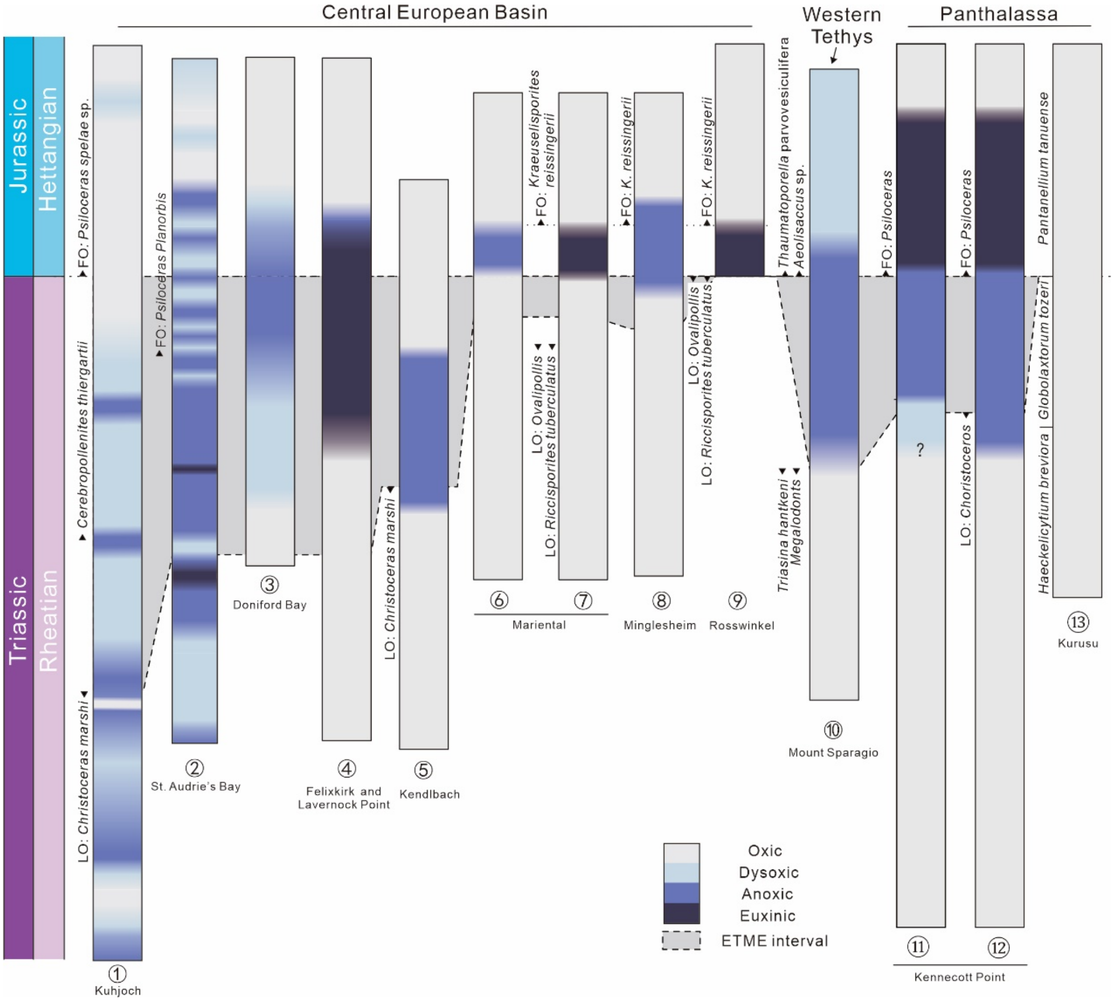

Fig. 5. Global correlation of seafloor redox conditions during the Triassic-Jurassic transition. Sections: 1 = Kuhjoch, Austria (this study); 2 = St. Audrie's Bay, UK (this study); 3 = Doniford Bay, UK (Paris et al., 2010; $\delta^{15}N$); 4 = Felixkirk and Lavernock Point, UK (Beith et al., 2021; biomarker); 5 = Kendlbach, Austria (Pálfy and Zajzon., 2012; rare Earth elements); 6 = Mariental, Germany (Luo et al., 2018; sulfur isotopes); 7 = Mariental, Germany (Richoz et al., 2012; biomarker); 8 = Minglesheim, Germany (Luo et al., 2018; sulfur isotopes); 9 = Rosswinkel, Luxembourg (Richoz et al., 2012; biomarker); 10 = Mount Sparagio, Italy (He et al., 2020, 2022b; $\delta^{34}S_{CAS}$ and I/(Ca+Mg)); 11 = Kennecott Point, Canada (Schoepfer et al., 2016; $\delta^{15}N$); 12 = Kennecott Point, Canada (Kasprak et al., 2015; biomarker); 13 = Kurusu, Japan (Fujisaki et al., 2020; $\delta^{15}N$). Abbreviations: LO: last occurrence; FO: first occurrence. The ETME interval is

constrained by the LO of the ammonite *Christoceras marshi* and the FO of *Psiloceras spelae* in the GSSP section at Kuhjoch. Question marks denote probable anoxic/dysoxic conditions.

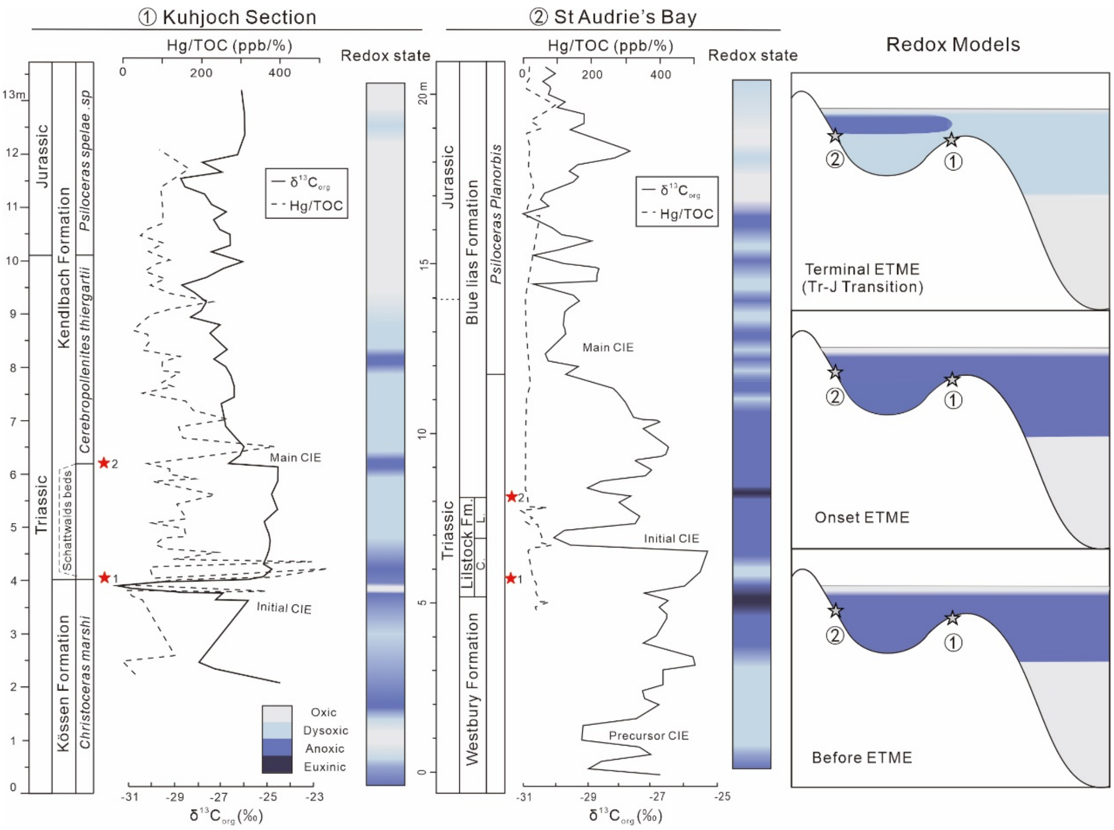

Fig. 6. $\delta^{13}C_{org}$ (solid line), Hg/TOC (dashed line), and inferred records of marine redox (modified after Fujisaki et al., 2020) through the ETME interval at St. Audrie's Bay and Kuhjoch. Hg/TOC data is from Percival et al. (2017); $\delta^{13}C_{org}$ data is from Hesselbo et al. (2002; St. Audrie's Bay) and Ruhl et al. (2009; Kuhjoch). Stars 1 and 2 represent the two extinction pulses in these sections according to Wignall and Atkinson (2020). C = Cotham Member; L = Langport Member.